

# Evolution of N/O ratios in galaxies from cosmological hydrodynamical simulations

Fiorenzo Vincenzo<sup>1\*</sup> & Chiaki Kobayashi<sup>1†</sup>

<sup>1</sup>Centre for Astrophysics Research, University of Hertfordshire, College Lane, Hatfield, AL10 9AB, UK

Accepted 2018 April 20. Received 2018 March 20; in original form 2018 January 22

## ABSTRACT

We study the redshift evolution of the gas-phase O/H and N/O abundances, both (i) for individual ISM regions within single spatially-resolved galaxies and (ii) when dealing with average abundances in the whole ISM of many unresolved galaxies. We make use of a cosmological hydrodynamical simulation including detailed chemical enrichment, which properly takes into account the variety of different stellar nucleosynthetic sources of O and N in galaxies. We identify 33 galaxies in the simulation, lying within dark matter halos with virial mass in the range  $10^{11} \leq M_{\text{DM}} \leq 10^{13} M_{\odot}$  and reconstruct how they evolved with redshift. For the local and global measurements, the observed increasing trend of N/O at high O/H can be explained, respectively, (i) as the consequence of metallicity gradients which have settled in the galaxy interstellar medium, where the innermost galactic regions have the highest O/H abundances and the highest N/O ratios, and (ii) as the consequence of an underlying average mass-metallicity relation that galaxies obey as they evolve across cosmic epochs, where – at any redshift – less massive galaxies have lower average O/H and N/O ratios than the more massive ones. We do not find a strong dependence on the environment. For both local and global relations, the predicted N/O–O/H relation is due to the mostly secondary origin of N in stars. We also predict that the O/H and N/O gradients in the galaxy interstellar medium gradually flatten as functions of redshift, with the average N/O ratios being strictly coupled with the galaxy star formation history. Because N production strongly depends on O abundances, we obtain a universal relation for the N/O–O/H abundance diagram whether we consider average abundances of many unresolved galaxies put together or many abundance measurements within a single spatially-resolved galaxy.

**Key words:** galaxies: abundances — galaxies: evolution — ISM: abundances — stars: abundances — hydrodynamics

## 1 INTRODUCTION

Elemental abundances are widely used in astrophysics to constrain the star formation history (SFH) of galaxies (e.g., Kobayashi 2016). An example of a SFH chemical abundance diagnostic is given by  $[\alpha/\text{Fe}]^1$ ; from the observed  $[\alpha/\text{Fe}]$ – $[\text{Fe}/\text{H}]$  relations, chemical evolution models have demonstrated that the various constituents of our Galaxy (halo, bulge, thick and thin disc) formed on different typical time scales (see, for example, Chiappini et al. 1997; Grieco et al. 2012; Brusadin et al. 2013; Micali et al. 2013; Spitoni et al. 2016; Grisoni et al. 2017); furthermore, by making use of the  $[\alpha/\text{Fe}]$  ratio estimated from spectral indices, chemical evo-

lution models have depicted early-type elliptical galaxies as forming from a short and intense burst of star formation in the past, in agreement with observations (Matteucci 1994; Thomas et al. 2003; Pipino & Matteucci 2004; Taylor & Kobayashi 2015a,b; Kriek et al. 2016; De Masi et al. 2018). The observed  $[\alpha/\text{Fe}]$ – $[\text{Fe}/\text{H}]$  diagram can be effectively used as a SFH diagnostic (i) firstly, because  $\alpha$ -elements and Fe are mostly released on different typical time scales by core-collapse and Type Ia Supernovae (SNe), respectively, and (ii) secondly, because the nucleosynthesis of  $\alpha$ -elements in stars is not correlated with their Fe abundance (Kobayashi et al. 2006).

In the star forming disc galaxies, however, it is not possible to measure iron abundances. For this reason, the O/H elemental abundance as well as the N/O<sup>2</sup> abundance ratio are among the most measured metallicity proxies in the interstellar medium (ISM). Current Galactic and extragalactic spectroscopic surveys such as MaNGA

\* f.vincenzo@herts.ac.uk

† c.kobayashi@herts.ac.uk

<sup>1</sup> By  $\alpha$ -elements we usually mean O, Mg, Ne, Si, S, Ca. The square bracket notation for the stellar chemical abundances is defined as follows:  $[X/Y] = \log(N_X/N_Y)_* - \log(N_X/N_Y)_{\odot}$ , where  $N_X$  and  $N_Y$  represent the number density of the chemical elements  $X$  and  $Y$ , respectively.

<sup>2</sup> For brevity, we use the following notation:  $\text{N/O} \equiv \log(\text{N/O})_{\text{gas}}$  and  $\text{O/H} \equiv \log(\text{O/H})_{\text{gas}} + 12$ , for the gas-phase chemical abundances.

(Bundy et al. 2015) are capable of reaching resolutions which were unimaginable only few decades ago. Large amounts of observational data are constantly being released, challenging theorists to develop models which can explain at the same time the variety of different physical observables nowadays available. One of the most important pieces of information we can extract from extragalactic spectroscopic surveys is the N/O–O/H diagram.

Historically, the N and O abundances have been measured for individual targets (e.g. HII regions or star forming regions) within a number of nearby galaxies (e.g., Garnett 1990; Vila Costas & Edmunds 1993; Izotov & Thuan 1999; Pilyugin et al. 2010; Berg et al. 2016; Magrini et al. 2017); then large-scale spectroscopic surveys have improved the statistics considerably, where chemical abundances have been measured from the integrated galaxy spectra (e.g. Andrews & Martini 2013, and references therein); finally, thanks to multi-object spectrographs and integral field unit (IFU) surveys, now it is possible to resolve the abundance patterns in star forming regions within a large number of galaxies (Pérez-Montero et al. 2016; Sánchez-Menguiano et al. 2016; Belfiore et al. 2017a). This growing amount of observational data has suggested the use of the N/O–O/H relation as an alternative SFH chemical abundance diagnostic of galaxies (Chiappini et al. 2005; Mollá et al. 2006; Vincenzo et al. 2016a). In near future, it will be possible to obtain these elemental abundances in high-redshift galaxies with JWST/NIRSpec and study the redshift evolution of the N/O–O/H relation.

Before studying the redshift evolution, it is important to understand the origin of the observed N/O–O/H relations in the local Universe. The observed relations have been obtained with O/H and N/O abundance measurements both (i) as *global* average values, measured from the galaxy integrated spectra and hence representative of unresolved galaxies, and (ii) as *local* abundance measurements in resolved HII or star forming regions within single, spatially-resolved external galaxies; these two cases are conceptually different with respect to each other and may give rise – in principle – to different N/O–O/H relations.

All the chemical elements with atomic number  $A \geq 12$  in the cosmos are synthesised in stellar interiors either during the quiescent phases of hydrostatic burning or through explosive nucleosynthesis during SN explosions (Arnett 1996). If a theoretical model is to make predictions about the chemical abundances coming from the analysis of stellar spectra, the chemical enrichment feedback from star formation activity must be properly included in the theoretical machinery by taking into account the variety of different nucleosynthesis sources which can actually produce a given chemical element  $X$ ; the different distributions of delay times between the formation of each astrophysical source and its death must also be taken into account (see Matteucci 2001, 2012; Pagel 2009 for exhaustive reviews on the subject).

Detailed chemical evolution of galaxies have mostly been studied by making use of one-zone models (e.g. Henry et al. 2000; Chiappini et al. 2005; Vincenzo et al. 2016a, but see also Vangioni et al. 2017, where a one-zone model has been embedded in a cosmological framework), which are based on the so-called instantaneous mixing approximation. However, in a real galaxy, chemical enrichment is inhomogeneous, which is important if we want to constrain the SFH from  $X/Y$  abundance ratio diagrams (Kobayashi & Nakasato 2011). Cosmological chemodynamical simulations are nowadays the best tools to shed light on how the SFH took place in different galaxies. These simulations are also key to understanding how chemical elements are synthesised, released and later distributed within galaxies, because they are able

to address the large amounts of data which are already available or about to come. In fact, cosmological chemodynamical simulations can provide a unifying picture for the formation and evolution of the many different populations of galaxies in the Universe (see, for example, Maio & Tescari 2015).

An advantage of using chemodynamical simulations is that one can predict both local and global relations for a large sample of simulated galaxies; another advantage is that one can naturally have chemical abundance gradients as functions of the galactocentric distance within the ISM of the simulated galaxies. By using chemical abundance measurements from the Cepheids (Andrievsky et al. 2002; Luck et al. 2003; Luck & Lambert 2011; Korotin et al. 2014; Genovali et al. 2015), planetary nebulae (Maciel & Koppen 1994; Costa et al. 2004; Stanghellini et al. 2006; Gutenkunst et al. 2008) or HII regions (Deharveng et al. 2000; Esteban et al. 2005; Rudolph et al. 2006; Fernández-Martín et al. 2017; Esteban et al. 2017) many observational works have shown, for example, that O/H in our Galaxy steadily diminishes when moving outwards as a function of the galactocentric distance, but radial gradients have been observed by those works also for other chemical elements; furthermore, Belfiore et al. (2017a) have shown that the N/O ratios can vary as functions of both the galactocentric distance and stellar mass, when considering a large sample of nearby galaxies in the MaNGA survey.

Historically, multi-zone chemical evolution models have been constructed to reproduce the observed radial metallicity gradients in the Galactic disc by assuming the so-called “inside-out scenario”, according to which the innermost (most metal-rich) Galactic regions assembled on much shorter typical timescales than the outermost (most metal-poor) ones, namely by assuming that the Galaxy formed *from the inside out* (see, for example, Chiappini et al. 2001; Cescutti et al. 2007; Magrini et al. 2009; Spitoni & Matteucci 2011). Chemical evolution models with inside-out growth of the disc and the star formation efficiency being modulated by the angular velocity of the gas predict a flattening of the radial metallicity gradients as a function of time (Portinari & Chiosi 1999; Boissier & Prantzos 2000); also chemodynamical simulations usually predict a flattening of the radial metallicity gradients as a function of time (see Kobayashi & Nakasato 2011; Pilkington et al. 2012; Gibson et al. 2013 and references therein). Finally, there are chemical evolution models predicting an inversion of the radial metallicity gradients at high redshift, corroborated by some observational findings (see Cresci et al. 2010; Werk et al. 2010; Queyrel et al. 2012; Mott et al. 2013, but also Schönrich & McMillan 2017 for a critical discussion).

In this work, we show the results of our cosmological chemodynamical simulation including the latest stellar nucleosynthesis yields; we investigate both (i) local and (ii) global N/O–O/H relations, i.e. (i) the relations obtained of individual targets *within* single spatially-resolved galaxies and (ii) the relations obtained with average abundances for the whole ISM of many unresolved galaxies put together. If the predicted relations follow a similar trend in the N/O–O/H diagram, we try to understand the causes of this in galaxies. Moreover, we show our predictions for the redshift evolution of the O/H and N/O radial gradients of a sample of galaxies in our cosmological simulation; finally, we show how the simulated galaxies move in the N/O–O/H, stellar mass–O/H and stellar mass–N/O diagrams as they evolve across cosmic epochs, fully exploiting the predictive power of a cosmological hydrodynamical simulation. We would like to note again that only by making use of chemodynamical simulations can we study both *local* and *global* evolution of chemical abundances, and that cosmological simulations allow

us to study the effect of environment on the chemical evolution of galaxies as well.

Our work is organised as follows. In Section 2 we summarise the main assumptions of our model and the analysis method of the simulation. In Section 3 we present the results of our study. We first discuss the origin of the local and global N/O–O/H relations for nearby galaxies, and then show the redshift evolution and the environmental dependence in Section 3.4. Finally, in Section 4 we draw our conclusions.

## 2 SIMULATION MODEL AND METHODS

Our simulation code is based on the GADGET-3 code (Springel 2005) and relevant baryon physics is included, namely UV background heating, metal-dependent radiative cooling, star formation, thermal stellar feedback, and chemical enrichment from asymptotic giant branch (AGB) stars, core-collapse and Type Ia supernovae (SNe). Therefore, the star formation activity within the ISM of galaxies is affected both by the thermal energetic feedback and by the chemical enrichment of star particles through stellar winds and SN explosions (see Kobayashi 2004; Kobayashi et al. 2007; Kobayashi & Nakasato 2011; Taylor & Kobayashi 2014 for a detailed description of the model).

In summary, we evolve a cubic volume of the standard  $\Lambda$ -cold dark matter Universe with side  $10 \text{ Mpc } h^{-1}$ , periodic boundary conditions, and the cosmological parameters being given by the nine-year Wilkinson Microwave Anisotropy Probe (Hinshaw et al. 2013);  $\Omega_0 = 0.28$ ,  $\Omega_\Lambda = 0.72$ ,  $\Omega_b = 0.046$ ,  $H_0 = 100 \times h = 70 \text{ km }^{-1} \text{ Mpc}$ , and  $\sigma_8 = 0.82$ . The mass resolution of our simulation is  $M_{\text{DM}} \approx 3.097 \times 10^7 h^{-1} M_\odot$  for the dark matter (DM) component and  $M_{\text{gas}} = 6.09 \times 10^6 h^{-1} M_\odot$  for the gas fluid. Finally, in our simulation we assume a gravitational softening length  $\epsilon_{\text{gas}} \approx 0.84 h^{-1} \text{ kpc}$ , in comoving units.

The initial conditions of our simulation are the same as in Kobayashi et al. (2007), but with updated cosmological parameters and better resolution; in particular, we assume initial conditions giving rise to a standard field at redshift  $z = 0$ , with no strong central concentration of galaxies. Our initial conditions are different from those in Taylor & Kobayashi (2014).

### 2.1 Chemical enrichment model

According to their mass and metallicity, stars at their death pollute the ISM of galaxies with different fractions of a given chemical element. We cannot resolve single stars in our simulation, hence we assume that each star particle represents a simple stellar population (SSP) with fixed age and chemical composition. Then we assume that all the embedded stars within each single SSP have a universal mass-spectrum at their birth which follows the Kroupa (2008) initial mass function (IMF), as defined in the stellar mass range  $0.01 \leq m \leq 120 M_\odot$ . As each given SSP gets older and older as a function of cosmic time, embedded stars with lower and lower mass enrich the surrounding gas particles with their nucleosynthetic products; the number of dying stars within a given SSP at the time  $t$  is given by the assumed IMF and SSP mass, while the enrichment time of a star with mass  $m$  and metallicity  $Z$  is given by the assumed stellar lifetimes,  $\tau(m, Z)$ ; in this work, we assume the stellar lifetimes of Kobayashi (2004), which are both metallicity- and mass-dependent.

In our simulation, the stellar nucleosynthetic yields are the

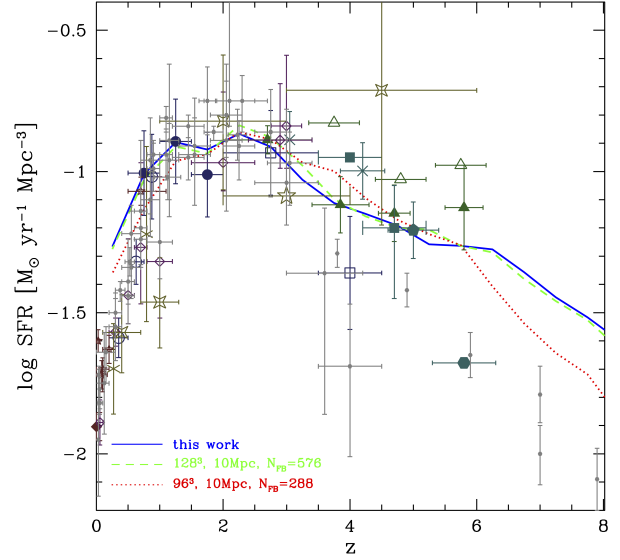


**Figure 1.** The predicted cosmic SFR as a function of redshift from different cosmological hydrodynamical simulations. The blue solid line corresponds to the predictions of the simulation of this work, with chemical enrichment including failed SNe; the green long dashed line to the same simulation as in this work but without failed SNe (original Kobayashi et al. 2011 stellar yields); finally, the red dotted line corresponds to the prediction of a similar simulation. The observational data are taken from Madau & Dickinson (2014, small grey points) and from Kobayashi et al. (2007, see references therein).

same as in Kobayashi et al. (2011), which include the chemical enrichment of AGB stars and SN explosions. The effect of hypernovae is included in our simulation for stars with mass  $m \geq 25 M_\odot$  with the following metallicity-dependent hypernova fraction:  $\epsilon_{\text{HN}} = 0.5, 0.5, 0.4, 0.01$ , and  $0.01$  for  $Z = 0, 0.001, 0.004, 0.02$ , and  $0.05$ , respectively, which is necessary to match the observed elemental abundances in the Milky Way (Kobayashi & Nakasato 2011). We additionally assume that all stars with mass  $m \geq 25 M_\odot$  and metallicity  $Z \geq 0.02$  which are not hypernovae end up their lives as failed SNe (Smartt 2009; Müller et al. 2016) and pollute the galaxy ISM only with H, He, C, N and F, which are synthesised in the outermost shells of the SN ejecta; the other chemical elements (including O) are assumed to fall back into the black hole, hence they are not expelled by the star into the surrounding ISM (see also Vincenzo & Kobayashi 2018; Kobayashi et al., in prep.).

We assume that each galaxy SSP distributes thermal energy and stellar nucleosynthetic products to its closest 576 neighbour gas particles (with the smoothing kernel weighting). This value, together with the other parameters specified above, is chosen to match the observed cosmic star formation rate (SFR; Hopkins & Beacom 2006; Madau & Dickinson 2014). Figure 1 shows the predicted cosmic SFR history of our simulation with failed SNe (blue solid line), as compared to the same simulation but with the original yields from Kobayashi et al. (2011, green long dashed line) without failed SNe. There is no significant difference in the cosmic SFRs and in the basic properties of the galaxies such as mass and morphology. The red dotted line in Figure 1 shows the predictions for the cosmic SFR of a similar simulation but with lower resolution ( $2 \times 96^3$  particles) than in this work ( $2 \times 128^3$  particles);

an agreement between the two can be only found by assuming a different number of feedback neighbour particles,  $N_{\text{FB}}$ . In particular, by increasing the resolution and keeping  $N_{\text{FB}}$  constant, ISM regions with higher and higher densities can be resolved and the SN feedback affects smaller regions around each given star particle; therefore, to obtain similar results in simulations with higher resolution,  $N_{\text{FB}}$  should be increased accordingly (Kobayashi et al. 2007).

Although our resolution is good enough to study radial gradients of chemical abundances in galaxies, it is not possible to resolve the small-scale physics within star-forming clouds and SN ejecta in galaxy simulations; for this reason, chemical enrichment is included by computing the contribution from each single star particle, depending on the metallicity. Therefore the chemical feedback can vary as a function of time and location within the galaxy (Kobayashi 2004; Kobayashi & Nakasato 2011). We remark on the fact that the evolution of the elemental abundance ratios in the ISM is mainly driven by the difference in the age and metallicity of the enrichment sources, being less affected by the uncertainty in the ISM metallicity due to the limited resolution.

Since in this paper we focus on the evolution of the N/O ratio in galaxies, we briefly recall here how O and N are synthesised by stars in galaxies (see also Kobayashi et al. 2011; Vincenzo et al. 2016a for more details). First of all, both N and O can be produced by massive stars, with mass  $m > 8 M_{\odot}$ , dying as core-collapse SNe on short typical time scales after the star formation event ( $\lesssim 30$  Myr); in this case, stellar evolutionary models predict N to be mainly produced as a secondary element in massive stars, in the CNO cycle at the expense of C and O nuclei already present in the gas mixture at the stellar birth. One-zone chemical evolution models showed that on its own, the “secondary” N component from massive stars is not sufficient to reproduce the observed N/O plateau in our Galaxy at very low metallicity (Matteucci 1986; Chiappini et al. 2005, 2008). Therefore, following the original suggestion of Matteucci (1986), many one-zone models assumed an additional primary N production by massive stars to reproduce the observed N/O plateau at very low metallicity (Pettini et al. 2002, 2008; Spite et al. 2005; Pilyugin et al. 2010), which is however highly scattered. In our simulation, we do not assume any additional primary N production for massive stars.

Low- and intermediate-mass (LIM) stars, with mass in the range  $4 \lesssim m \lesssim 8 M_{\odot}$ , are dominant stellar nucleosynthesis sources of N, when experiencing the AGB phase (see, for example, Ventura et al. 2013, 2017 for more details). Most of the nitrogen from AGB stars is secondary and its stellar yields steadily increase as functions of the initial stellar metallicity. Note that, however, there may be also a primary N component that can be important in the chemical evolution of galaxies at very low metallicity, which is predicted when hot-bottom burning occurs in conjunction with the so-called third dredge-up (see also Vincenzo et al. 2016a and reference therein).

## 2.2 Analysis of the simulation

From our cosmological simulation, we create a catalogue of 33 stellar systems at redshift  $z = 0$ , all embedded within dark matter (DM) halos with virial mass in the range  $10^{11} \leq M_{\text{DM}} \leq 10^{13} M_{\odot}$ ; we make use of the ROCKSTAR friend-of-friends group-finding algorithm with adaptive hierarchical refinement to determine all the DM halos in the simulation (Behroozi et al. 2013). The 33 stellar systems of our catalogue span a variety of different star formation histories (SFHs) and consequently show different chem-

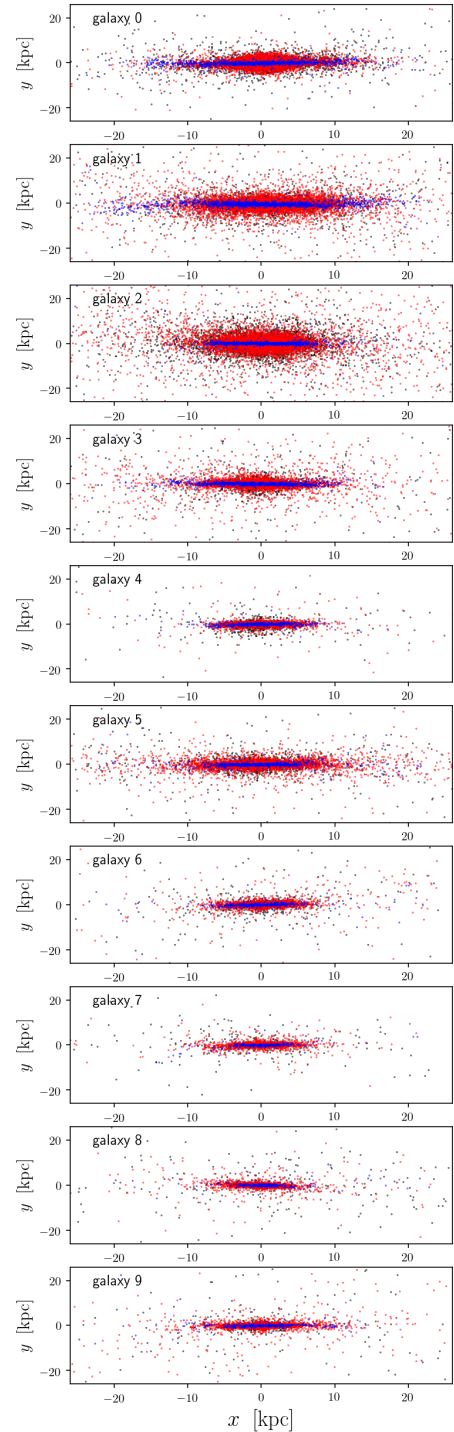


**Figure 2.** Our ten reference galaxies when viewed edge-on. Black points correspond to the older stellar populations (> 90 per cent in the cumulative age distribution function); blue points to younger star particles (< 10 per cent in the cumulative age distribution function); finally, red points correspond to intermediate-age stellar populations which lie between 10 and 90 per cent in the cumulative age distribution function.

ical evolution histories from their formation epoch. For each stellar system at redshift  $z = 0$  in our catalogue, we retrieve the main physical and chemical properties of all its star and gas particles going back in redshift, by means of a simple searching algorithm (each particle in the simulation is univocally characterised by an ID number). At all redshifts, each galaxy in our catalogue is defined as follows.

(i) At any given time  $t_1$  in the past, we fit with Gaussian functions the normalised density-weighted distributions of the  $x$ ,  $y$  and  $z$  coordinates of all the gas particles within the galaxy, which have been retrieved from the simulation snapshot at a time shortly after  $t_2 = t_1 + \Delta t$ ; then we consider in our analysis all the star and gas particles at the time  $t_1$  in the simulation which lie within  $4\sigma$  from the centre of the three Gaussians. Therefore, in the presence of merger events, we choose to follow the stellar system with the highest gas densities.

(ii) If the fitting procedure fails at a given redshift (usually corresponding to high velocity encounters or minor/major mergers), we broaden our criteria and consider at that redshift all the gas and star particles which lie within 20 kpc from the centre of mass of the star particles which have been retrieved from the subsequent simulation time step.

By following the analysis as described above, we can study the evolution of the galaxy physical properties continuously as functions of redshift with an automated algorithm. The small fluctuations in the predicted evolution of the average galaxy properties are mostly due to an imperfect centring on the galaxy main body, particularly associated with merging episodes with other stellar systems.

### 3 RESULTS

In this Section, we present our new results from the analysis of the cosmological hydrodynamical simulation described in Section 2. In this work, we select ten representative star forming disc galaxies from our catalogue, so that these reference galaxies have a range of characteristic SFHs. All of our ten reference galaxies lie within DM halos with virial masses in the range  $10^{11} \leq M_{\text{DM}} \leq 10^{12} M_{\odot}$ . In the first part of this Section, we show our predictions for the gas-phase O/H–N/O abundance patterns in our reference galaxies. In the second part, we show how the average O/H and N/O abundance ratios evolve with time when considering our entire sample of 33 galaxies.

#### 3.1 Star formation history of the reference disc galaxies

Our ten reference galaxies are shown in Figure 2, as viewed edge-on. Different colours in Figure 2 correspond to galaxy stellar populations with different age; in particular, the black points correspond to the older galaxy stellar populations ( $> 90$  per cent in the cumulative age distribution function); blue points to younger star particles ( $< 10$  per cent in the cumulative age distribution function); finally, red points correspond to intermediate-age stellar populations which lie between 10 and 90 per cent in the cumulative age distribution function.

In Figure 3, we show the distribution of the total stellar mass of our ten reference galaxies at redshift  $z = 0$  as a function of the stellar age. When passing from Galaxy 0 to Galaxy 9, the stellar mass growth history becomes more concentrated towards later and later epochs. While most of the galaxies have smooth SFHs, Galaxy 1 undergoes a major merger of two stellar systems with average

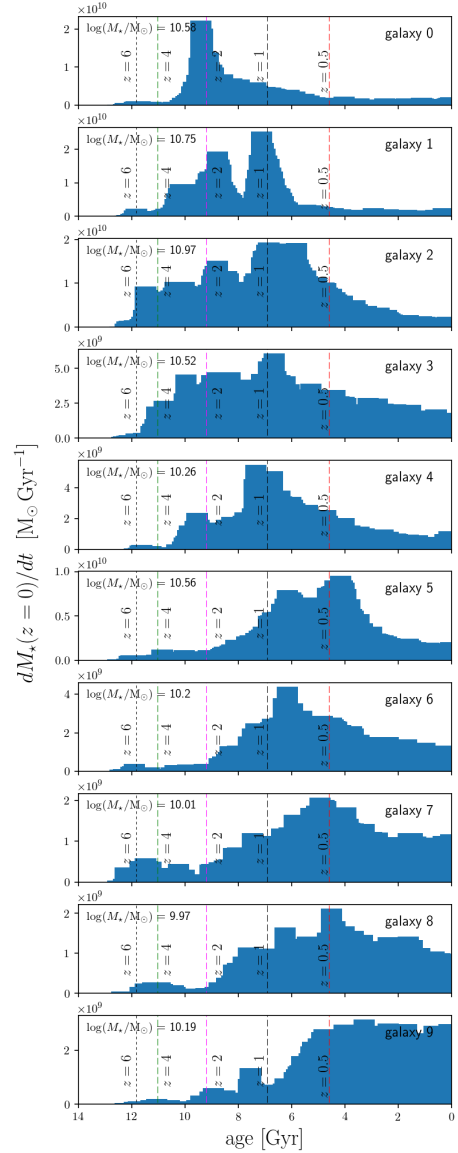


**Figure 3.** The stellar mass distribution function of our ten reference galaxies as functions of the stellar birth time. The area under the predicted distribution corresponds to the total galaxy stellar mass at redshift  $z = 0$ . From top to bottom, our ten reference galaxies have decreasing average stellar ages. The figure can be read as the fraction of the present-day galaxy stellar mass coming from each given age bin in the past. In the upper corner on the left we report for each panel the total galaxy stellar mass at  $z = 0$ .

ages peaking at  $\approx 9$  and 7 Gyr ago. After the onset of star formation at  $z \sim 6$ , Galaxies 2 and 3 had a relatively rapid increase of SFR, while the other galaxies had a slow start with very low SFR at  $z < 4$ . Galaxy 9 is the youngest and maintains a high SFR at the present epoch.

#### 3.2 O/H–N/O relations within single resolved galaxies

In Figure 4, the predicted gas-phase  $\log(\text{O/H})$ – $\log(\text{N/O})$  relation of individual ISM regions (blue points) in our ten reference galaxies is compared to the observations in the local Universe (Dopita et al. 2016; Belfiore et al. 2017a). We remark on the fact that the majority of the gas particles in our ten reference galaxies lie on a thin

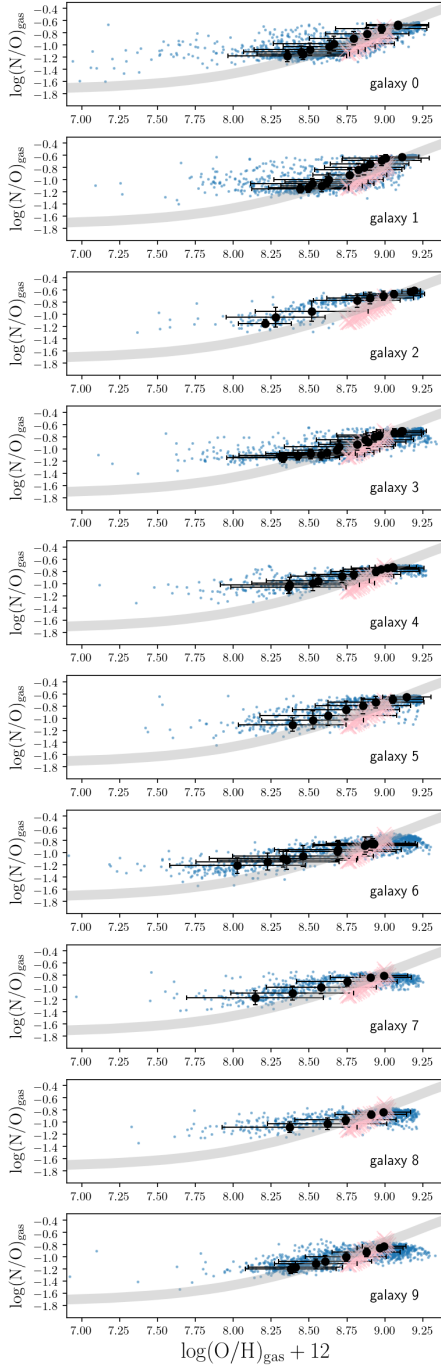


**Figure 4.** The predicted O/H–N/O abundance diagrams in our ten reference galaxies (blue points for each ISM location in the galaxy). The black points with the error bars correspond to the average O/H and N/O with the corresponding  $1\sigma$  deviation, as derived by dividing our simulated galaxies in many concentric annuli and measuring the average gas-phase abundances within each annulus (in this case we only consider gas particles which lie within three times the galaxy half-mass radius, as computed from the stellar mass radial profile); blue points at higher O/H abundances lie in the inner galactic regions. We compare our simulation with the observed average relation of [Dopita et al. \(2016\)](#), grey solid line; see references therein) and the observed data from the MaNGA survey of [Belfiore et al. \(2017a\)](#), pink symbols) for nearby disc galaxies with stellar mass in the range  $9.5 \leq \log(M_*/M_\odot) \leq 11.0$  dex.

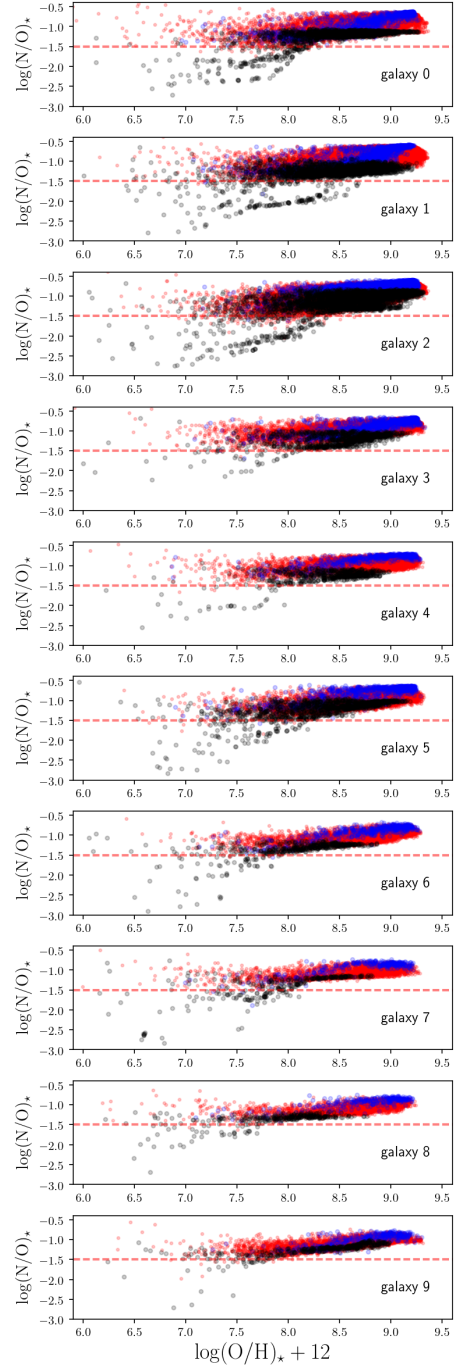


**Figure 5.** The predicted O/H–N/O abundance diagrams in the different stellar populations of our ten reference galaxies, from top to bottom. The black points represent the older stellar populations ( $> 90$  per cent in the cumulative age distribution function) in our reference galaxies; blue points to younger star particles ( $< 10$  per cent in the cumulative age distribution function); finally, red points correspond to intermediate-age stellar populations which lie between 10 and 90 per cent in the cumulative age distribution function. The red dashed line indicates the suggested average low-metallicity N/O-plateau at  $\log(N/O) \approx -1.5$  dex, as predicted by chemical evolution models with pure primary N production by massive stars.

disc at the present time. The black points with the error bars represent the average O/H and N/O abundances with the corresponding  $1\sigma$  standard deviation as predicted when dividing the galaxy in different concentric annuli of galactocentric distance and computing the average gas-phase O/H and N/O ratios therein; in this case, we only consider gas particles which lie within three times the galaxy half-mass radius, as computed from the stellar mass radial profile.

The predicted N/O–O/H relation within all our reference galaxies qualitatively agrees with the observed N/O and O/H abundance measurements of Belfiore et al. (2017a, pink symbols) from a large sample of spatially-resolved galaxies in the MaNGA survey. Our simulation also nicely follows the observed relation as derived by Dopita et al. (2016, grey line), obtained by compiling data from Milky Way metal-poor stars (Israelian et al. 2004; Spite et al. 2005), resolved HII regions in blue compact galaxies (Izotov & Thuan 1999) and local B stars (Nieva & Przybilla 2012). At low metallicity, although we do not have many points, our predictions give slightly larger N/O, which may be due to the difference in the targets. We note that the observed slopes of N/O vs. O/H of Dopita et al. (2016) and Belfiore et al. (2017a) differ from each other because of well-known uncertainties in the abundance measurements, mostly due to the assumed calibration (see, for example, Kewley & Ellison 2008, but also the discussion in Belfiore et al. 2017a).

In our simulations, the observed increasing trend of N/O vs. O/H is reproduced with failed SNe. If we do not assume failed SNe (namely, had we assumed the original Kobayashi et al. 2011 stellar yield set), we predict almost flat trends and hence dramatically fail in reproducing the observed increasing trend of N/O vs. O/H at high metallicity (see Vincenzo & Kobayashi 2018). On average, within all our reference galaxies in Figure 4, we predict that the galactic annuli with the largest O/H abundances lie in the innermost galactic regions and have also the largest N/O ratios; conversely, the galactic regions with the lowest O/H abundances are preferentially concentrated outwards and have the lowest N/O ratios.

At redshift  $z = 0$ , we have only a few low-metallicity components in the gas-phase of the galaxy ISM. However, these are predicted to be common at higher redshift, at the earliest evolutionary stages of the galaxies (see Vincenzo & Kobayashi 2018). At redshift  $z = 0$ , the low-metallicity components can be seen more clearly in the oldest galaxy stellar populations; this is shown in Figure 5, where the different galaxy stellar populations are discriminated with different colours in the N/O–O/H diagram according to their formation time, by using the same criteria as in Figure 2.

At low metallicity, the majority of the older stellar population (black dots) show a flat trend as a function of metallicity. We recall here that a flat trend of N/O in our chemodynamical model is caused by inhomogeneous chemical enrichment, where a significant contribution of AGB stars appears at low O/H. Depending on the relative contribution between SNe and AGB stars, the exact value of the N/O ratios in the plateau may vary from galaxy to galaxy according to the galaxy formation time and SFH. At  $z = 0$ , this effect of inhomogeneous chemical enrichment is more important at the outskirts of our simulated galaxies because of the low SFRs (see Vincenzo & Kobayashi 2018). On the one hand, massive galaxies that have relatively fast star formation also show very low N/O ratios, below the plateau, for the oldest and metal-poor stellar populations; these values are roughly in agreement with the observations in damped Ly $\alpha$  (DLA) systems (Pettini et al. 2002, 2008), which are, however, also highly scattered (Zafar et al. 2014; Vangioni et al. 2017). On the other hand, the oldest and most metal-poor stellar populations in the less massive galaxies have  $\log(\text{N/O}) \sim -1.5$  dex, on average.

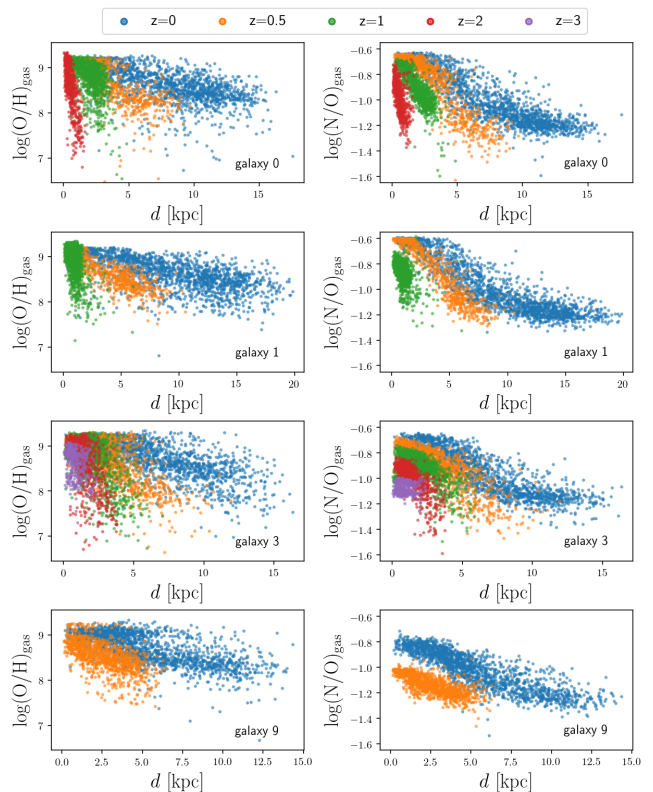


**Figure 6.** The predicted redshift evolution of the O/H (left panels) and N/O (right panels) gradients in the ISM of a sub-sample of four galaxies, as chosen from our ten reference galaxies.

In Figure 6, we show how the gas-phase  $\log(\text{O/H})$  and  $\log(\text{N/O})$  ratios vary as functions of the galactocentric distance and time within a sub-sample of our ten reference galaxies. Different colours correspond to different redshifts when the gradients are computed. Although there is a dispersion in the chemical abundances at any fixed galactocentric distance (particularly for the O/H abundances; see also the horizontal error bars in Figure 4), after the first star formation episode in the galaxy, we predict a flattening of the abundance gradients as a function of time, together with an inside-out growth of the galaxy disc. In particular, in the very early “protogalactic” evolutionary stages, we predict highly scattered and overall flat abundance gradients; then, as the first series of stellar populations form and the galaxy contextually accretes gas from the environment, steep gas-phase abundance gradients develop, which then gradually flatten as a function of time. The predicted flattening of the abundance gradients with time is in agreement with the predictions of previous chemodynamical simulations (e.g., Pilkington et al. 2012). Finally, the average O/H abundances at the centre do not show a strong redshift evolution, which is consistent with the observations in our Galactic bulge (Zoccali et al. 2008).

To explain our prediction of negative radial N/O gradients at redshift  $z = 0$ , we recall here that the main N-producers in galaxies are not low-mass stars (see also Section 2.1), with chemical composition reflecting the chemical abundances in the ISM, from which they were born quite recently. The fact that we predict negative radial gas-phase O/H gradients at  $z = 0$  makes the N-producers more metal-rich inside than outside. Since N is mainly synthesised as a secondary element (namely, the N stellar yields increase, on aver-

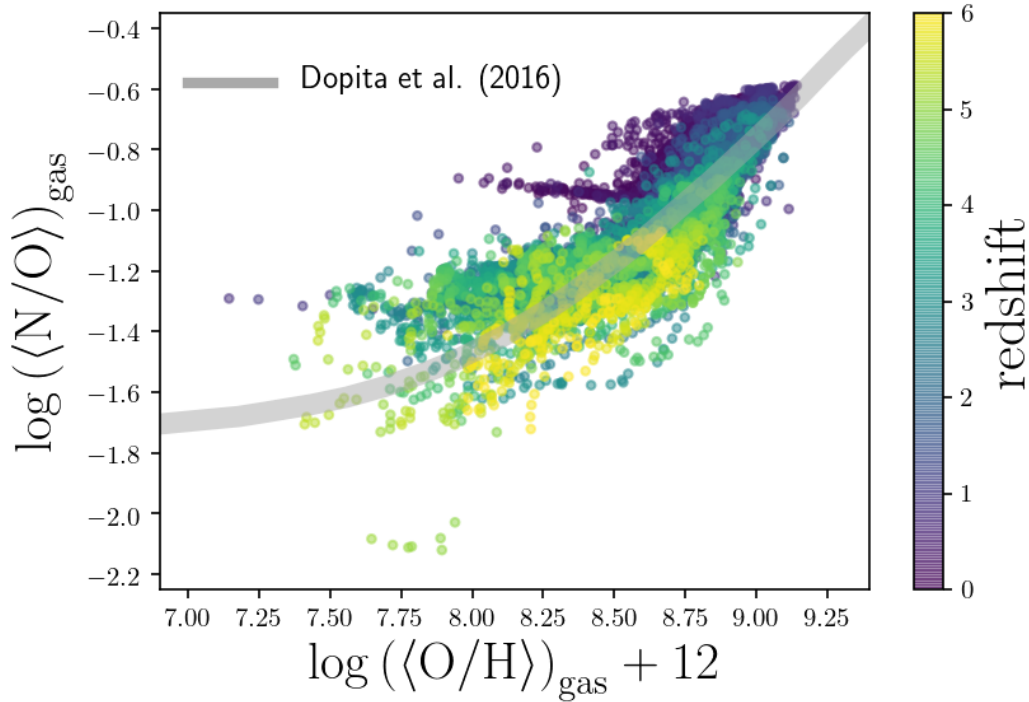


**Figure 7.** The redshift evolutionary tracks of all 33 galaxies in our catalogue in the O/H–N/O diagram. The abundances in the figure correspond to SFR-weighted averages in the gas-phase of the ISM. The colour coding represents the redshift.

age, as functions of the stellar metallicity), there is a corresponding increase of the average gas-phase N/O ratios when moving towards the inner galactic regions along the disc, where we predict the largest metallicities. In summary, the *local* O/H–N/O relation in Figure 4 can be explained as the consequence of radial gradients in the disc within the galaxy ISM, as shown in Figure 6.

### 3.3 Global average N/O–O/H relation

In this Section, we show how all 33 galaxies of our catalogue move in the N/O–O/H, mass–O/H and mass–N/O diagrams as a function of their evolutionary time. We focus on the average SFR-weighted  $\log(\text{O}/\text{H})$  and  $\log(\text{N}/\text{O})$  ratios of the whole ISM in the galaxies.

The main results of our analysis are shown in Figure 7, where we have put together all 33 galaxies in our catalogue to show how they evolve in the N/O–O/H diagram; each point represents the SFR-weighted average  $\log(\text{O}/\text{H})$  and  $\log(\text{N}/\text{O})$  ratios in the ISM of each galaxy, and the colour coding indicates the redshift of the galaxy. We find that the galaxies in our catalogue follow tracks in the N/O–O/H diagram which agree with the average Dopita et al. (2016, solid grey line) relation. Although we do not have many points at very low average gas-phase O/H abundances in our reference galaxies at high redshift, the points around  $\log(\text{O}/\text{H}) \sim 7.5$  dex are in good agreement with the observations in DLA systems (Pettini et al. 2002, 2008; Zafar et al. 2014), in the halo stars of our Galaxy (Matteucci 1986; Spite et al. 2005), and in irregular dwarf galaxies (e.g. Berg et al. 2016), which exhibit  $\log(\text{N}/\text{O}) \approx -1.5$  dex with a large scatter around this value (see also Vincenzo & Kobayashi 2018).

In a given redshift interval, we predict that the highest N/O and O/H ratios are seen in the most massive galaxies. Therefore, the *global* N/O–O/H relation can be explained as being determined by

the galaxy stellar mass. To demonstrate this, in Figure 8 we show how all 33 galaxies of our catalogue evolve in the  $\log(M_*/M_\odot)$ – $\log(\langle\text{O}/\text{H}\rangle)$  diagram (top panel) and  $\log(M_*/M_\odot)$ – $\log(\langle\text{N}/\text{O}\rangle)$  diagram (bottom panel). Although there is a dispersion in the predicted average abundances, we predict well-defined correlations in the stellar mass–O/H and stellar mass–N/O diagrams in all redshift intervals. Compared with observations, our O/H and N/O abundances are systematically larger than the observed abundance measurements of Andrews & Martini (2013, grey points with error bars) from the Sloan Digital Sky Survey Data Release 7 (Abazajian et al. 2009, SDSS DR7); the offset between model and data might be due to (i) the assumed IMF when fitting the observed galaxy spectral energy distribution (SED), which mostly affects the galaxy stellar mass estimates, and/or (ii) the assumed calibration in the chemical abundance measurement, which can strongly affect the O/H abundances (see, for example, Kewley & Ellison 2008; Belfiore et al. 2017a). Our redshift evolution of the stellar mass–O/H relation is slightly weaker than in Taylor & Kobayashi (2016), which is due to the failed SN scenario assumed in this work. We note that the feedback from active galactic nuclei (AGNs) is not included in our simulation, however the effect of AGN feedback has been shown to be negligible for this relation (Taylor & Kobayashi 2015a,b).

Since the galaxy stellar mass strongly correlates with the average galaxy ISM metallicity, there is also a correlation between stellar mass and the average N/O ratio in the ISM, which is mostly due to the secondary behaviour of the N stellar yields from massive stars and AGB stars. In this way, we can explain the observed stellar mass–N/O relation of Andrews & Martini (2013) in the redshift range  $0.027 < z < 0.25$ , although there is an offset between model and data.

Finally, because we weight the global O and N abundances with the SFR, we show that the SFRs of our simulated galaxies

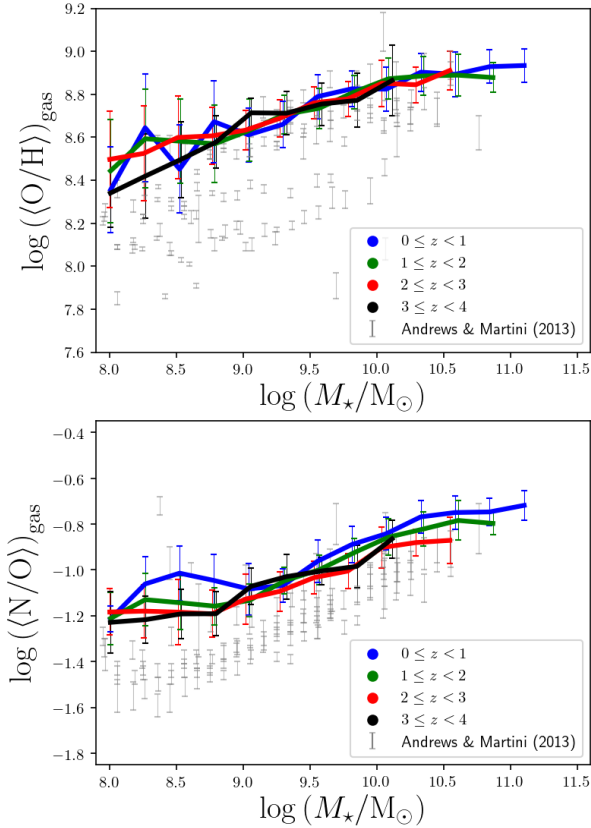


**Figure 8.** The redshift evolutionary tracks of all 33 galaxies in our catalogue in the stellar mass–O/H (top panel) and stellar mass–N/O (bottom panel) diagrams. As in Figure 7, the abundances in the figure correspond to SFR-weighted averages in the gas-phase of the ISM. Different colours correspond to predicted mass–O/H and mass–N/O relations at different redshift intervals, as specified in the legends of the figure. The solid lines correspond to the average relation when dividing our catalogue in different stellar mass bins, while the error bars correspond to the  $1\sigma$  standard deviation. The grey points with error bars in both panels correspond to the average observed abundance measurements of Andrews & Martini (2013) in the redshift range  $0.027 < z < 0.25$  from the SDSS DR7 (Abazajian et al. 2009).

are in good agreement with observations. In Figure 9, the predicted global SFR– $M_*$  relation at redshift  $z = 0$  in our galaxy catalogue (black points) is compared with the observed data from Cicone et al. (2017, grey points with error bars) and the observed average relation from Belfiore et al. (2017b), which is consistent with the Renzini & Peng (2015) relation. Although the scatter in the predicted average SFRs is large, our simulation qualitatively agrees with observations. Finally, we note that the red sequence cannot be produced without the feedback from AGNs (Taylor & Kobayashi 2015a,b).

### 3.4 N/O evolution in a cosmological context

Since the global N/O–O/H relation in Figure 7 is primarily driven by the mass-metallicity of galaxies, one may expect some environmental dependence. Although the environmental dependence of mass-metallicity relation is seen in some observational data (Ellison et al. 2009), it is not so clear in other works (e.g., Kacprzak et al. 2015; Pilyugin et al. 2017).

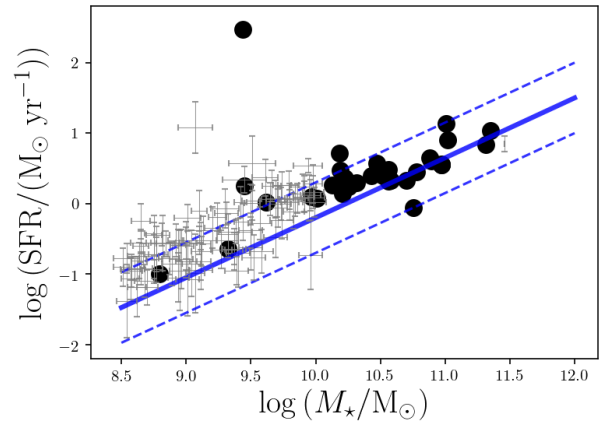


**Figure 9.** The  $\log(M_*/M_\odot)$ – $\log(\text{SFR}/(M_\odot \text{ yr}^{-1}))$  relation as predicted at redshift  $z = 0$  for our galaxy catalogue (black points) and compared with the observed data of Cicone et al. (2017, grey points with error bars) and the observed average relation of Belfiore et al. (2017b, blue solid line) with the corresponding  $1\sigma$  scatter (blue dashed lines).

In Figure 10, we show the effect of the environment on the evolution of galaxies in the N/O–O/H diagram. As the indicator, we use the distance to the fifth nearest halo identified in our cosmological simulation at  $z = 0$ , which represents the large-scale structures of galaxies very well (see Figure 5 of Taylor & Kobayashi 2017). High values of  $s_5$  for a given DM halo (which can typically be as high as  $\approx 0.9$  Mpc) indicate relatively low densities of galaxies in the local environment. The various points in Figure 10 represent the redshift evolutionary tracks in the N/O–O/H diagram as followed by all the galaxies in our catalogue with the colour coding indicating the  $s_5$  index. Note that the galaxies are over-plotted in the order of  $s_5$ .

By visually comparing Figures 7 and 10, it can be seen that the environmental dependence is much weaker than the redshift evolution; all galaxies follow the same N/O–O/H relation, indicating that the galaxy chemical evolution is self-regulated even with different SFHs. There may be a small environmental dependence seen, where the galaxies in the densest regions (with the lowest  $s_5$  values) can reach higher average N/O ratios by the present time at any fixed O/H abundance. We also find that these galaxies in the densest regions tend to show a larger scatter of evolutionary tracks in the N/O–O/H diagram. This may indicate that not only the star formation efficiency (i.e., O/H) but also chemical enrichment timescale (i.e., N/O) may be different depending on the environment. We should note, however, that this needs to be studied more with a large volume of simulations.

In contrast, there is a variation in the N/O evolution depending on the galaxy SFH. In Figure 11, we show our predictions for the redshift evolution of the average SFR-weighted  $\log(\text{O}/\text{H}) + 12$  and  $\log(\text{N}/\text{O})$  ratios in the gas-phase of our ten reference galaxies (in Figs. 2 and 3), at redshifts  $z \leq 2$  and for total stellar masses  $M_* \geq 10^8 M_\odot$ . First of all, we predict the average N/O ratios to increase, on average, in the galaxy ISM by the present; secondly, galaxies with a relatively smooth SFH, like galaxies 3–7, and 8, exhibit also a smooth increasing trend of the average gas-phase N/O ratio. Sudden bumps in the galaxy stellar mass growth history significantly affect the slope of the predicted N/O evolution, causing similar bumps in the predicted N/O evolution.

There are few observational studies in the literature which systematically attempted to measure N/O and O/H in galaxies at high

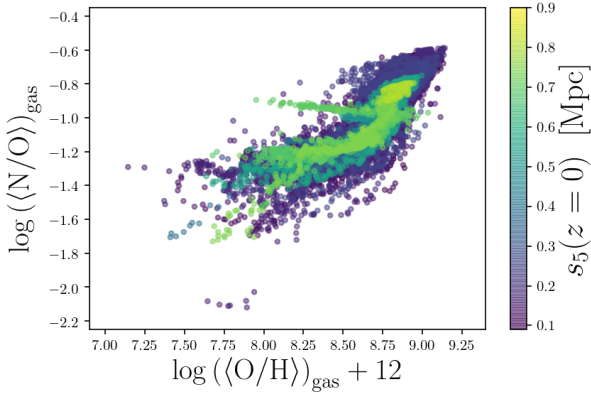


**Figure 10.** Same as Figure 7 but coloured with the 5th nearest distance  $s_5$  at  $z = 0$  to show the environmental dependence. Higher values of  $s_5$  indicate less dense environments.

redshifts; they mostly focused on AGN, gamma ray burst (GRB) or SN host galaxies, by making use of a detailed numerical modelling of the galaxy spectral energy distribution. Examples of such systematic studies are the series of works by Contini (2015, 2016, 2017a,b, 2018, but see also the previous works of the same author), which adopted the SUMA numerical code<sup>3</sup>, taking into account the combined effect of photoionisation and shocks (Contini & Aldrovandi 1983, 1986). In Figure 12, we compare the predictions of our simulation for the redshift evolution of  $\log(\text{O}/\text{H}) + 12$  and  $\log(\text{N}/\text{O})$  (top and bottom panels, respectively) with the measurements in GRB and SN host galaxies (red triangles and blue stars, respectively). Our simulation tends to have lower O/H and thus higher N/O than in observations especially at high redshifts. This is rather odd as it is the opposite from what we show in Figure 8. This observational dataset may not be straight-forwardly comparable to our simulation; some spectra in the catalogue of Contini (2016, 2017a,b) were taken in the very early phases after the SN explosion, before the SN ejecta disperse into the ambient ISM; this may eventually contaminate the abundance analysis, by leading to higher measured O/H abundances and hence lower N/O ratios. A similar tendency was reported for DLA systems, where GRB-DLA show higher metallicity than QSO-DLA at high redshifts (Cucchiara et al. 2015). In future, comparisons with unbiased large samples of galaxies will provide a more definitive test of our model predictions.

#### 4 CONCLUSIONS

In this work, we have demonstrated that our model is capable of reproducing the observed increasing trend of N/O vs. O/H at high metallicity in the nearby star forming galaxies, by introducing failed SNe in our cosmological chemodynamical simulation.

We have constructed a sample of 33 star forming disc galaxies at redshift  $z = 0$ , embedded within DM halos with virial mass in the range  $10^{11} \leq M_{\text{DM}} \leq 10^{13} M_{\odot}$ . We have analysed the detailed chemical evolution of the N and O abundances within ten reference galaxies of our catalogue, characterised by well distinct SFHs (Figure 3). We have also shown how all 33 galaxies in our catalogue evolve in the N/O–O/H, stellar mass–O/H and stellar mass–N/O

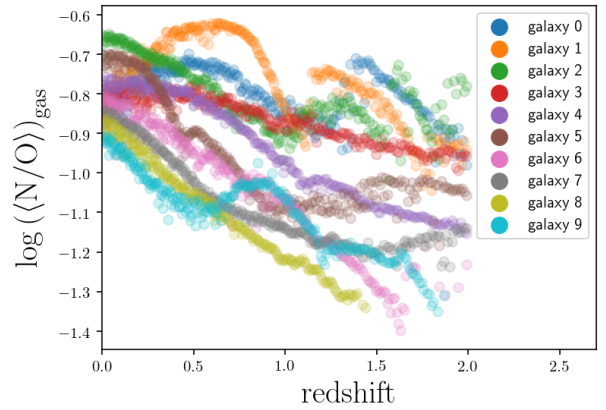


**Figure 11.** The predicted redshift evolution of the average SFR-weighted N/O ratios within our ten reference galaxies in Figs. 2 and 3.

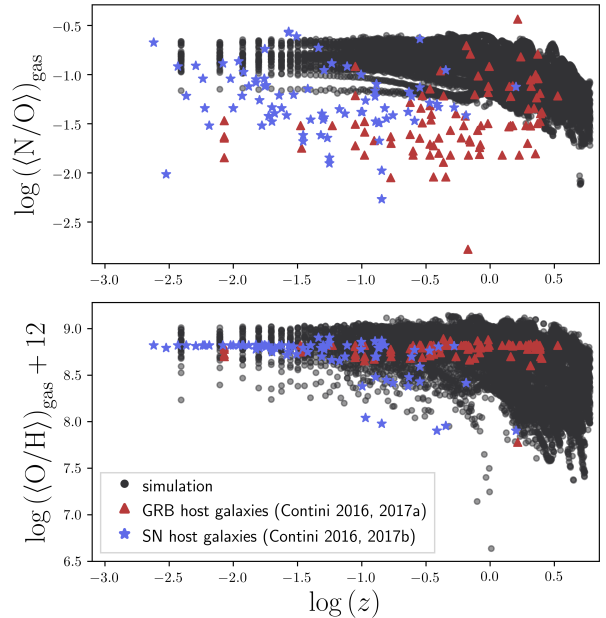


**Figure 12.** The predicted redshift evolution of N/O and O/H of all the galaxies in our catalogue (black circles in the top and bottom panels, respectively), comparing with available observations for SN host (blue stars) and GRB host (red triangles) galaxies (see the main text for more details).

diagrams, when considering SFR-weighted average abundances in the whole galaxy ISM. Our main conclusions can be summarised as follows.

(i) The observed increasing trend of N/O at high O/H in the individual ISM regions of spatially-resolved star forming disc galaxies (we have referred to it as *local* N/O–O/H relation in this work) can be explained as the consequence of metallicity gradients which have settled in the galaxy ISM, where the innermost regions possess both the highest O/H and the highest N/O ratios.

(ii) The *global* N/O–O/H relation when dealing with average abundances from the whole galaxy ISM is the consequence of an underlying mass-metallicity relation that galaxies obey as they evolve across the cosmic epochs. In this case, the predicted N/O–O/H relation is an average evolutionary trend which is followed by the chemical evolution tracks of all galaxies at almost any redshift.

<sup>3</sup> <http://wise-obs.tau.ac.il/~marcel/suma/index.htm>

(iii) We do not find a strong environmental dependence but find that galaxies follow the same *global* N/O–O/H relation independent of the environment ( $s_5$ ). However, galaxies in the densest environments at  $z = 0$  show a larger scatter along the relation, and thus can have higher N/O ratios at high O/H, than the galaxies in the least dense environments.

(iv) For both local and global relations, the increasing trend of N/O as a function of O/H is mainly due to the fact that N is mainly produced as secondary element at the expense of the C and O nuclei already present in the stars at their birth; the higher the initial stellar O/H abundance, the larger is the amount of synthesised N produced by stars.

(v) The average N/O ratios increase more rapidly in galaxies having SFHs concentrated at earlier cosmic epochs. Smooth stellar mass growth with time gives rise to smooth monotonic evolution of the average N/O ratios with redshift. Conversely, sudden bumps in the stellar mass growth history may also give rise to similar bumps in the  $z$ –N/O evolutionary tracks. Therefore, the redshift evolution of N/O in galaxies could be used to constrain the SFH of disc galaxies.

(vi) We predict that the O/H and N/O gradients in the ISM of galaxies flatten – on average – as functions of time, in agreement with previous studies on the metallicity gradient evolution in disc galaxies (e.g. Kobayashi & Nakasato 2011; Pilkington et al. 2012; Gibson et al. 2013); contextually, we predict also an inside-out growth of the galaxy as a function of time. In the very early “proto-galactic” evolutionary stages, we predict highly scattered and overall flat abundance gradients; then, as the first series of stellar populations form, steep gas-phase abundance gradients soon develop and then gradually flatten by the present time.

## ACKNOWLEDGMENTS

We thank an anonymous referee for his/her constructive comments and suggestions on the cosmological context. FV acknowledges funding from the UK Science and Technology Facility Council (STFC) through grant ST/M000958/1. This research has made use of the DiRAC high-performance computing (HPC) facility in the UK at Durham, supported by STFC and BIS; we also have made use of the University of Hertfordshire’s HPC facility for the simulation analysis. CK acknowledges PRACE for awarding her access to resource ARCHER based in the UK at Edinburgh. Finally, we thank Volker Springel for providing the code GADGET-3, Francesco Belfiore for providing the observed data set and for many stimulating discussions, and Roberto Maiolino and Philip Taylor for fruitful discussions.

## REFERENCES

Abazajian, K. N., Adelman-McCarthy, J. K., Agüeros, M. A., et al. 2009, *ApJS*, 182, 543–558  
 Andrews, B. H., & Martini, P. 2013, *ApJ*, 765, 140  
 Andrievsky, S. M., Kovtyukh, V. V., Luck, R. E., et al. 2002, *A&A*, 381, 32  
 Arnett, D. 1996, Princeton University Press  
 Behroozi P. S., Wechsler R. H., Wu, H.-Y. 2013, *ApJ*, 762, 109  
 Belfiore, F., Maiolino, R., Bundy, K., et al. 2015, *MNRAS*, 449, 867  
 Belfiore, F., Maiolino, R., Tremonti, C., et al. 2017, *MNRAS*, 469, 151  
 Belfiore, F., Maiolino, R., Bundy, K., et al. 2017, *arXiv:1710.05034*  
 Berg D. A., Skillman E. D., Henry R. B. C., Erb D. K., Carigi L., 2016, *ApJ*, 827, 126  
 Boissier, S., & Prantzos, N. 2000, *MNRAS*, 312, 398

Brusadin, G., Matteucci, F., & Romano, D. 2013, *A&A*, 554, A135  
 Bundy, K., Bershad, M. A., Law, D. R., et al. 2015, *ApJ*, 798, 7  
 Cescutti, G., Matteucci, F., François, P., & Chiappini, C. 2007, *A&A*, 462, 943  
 Chiappini, C., Matteucci, F., & Gratton, R. 1997, *ApJ*, 477, 765  
 Chiappini, C., Matteucci, F., & Romano, D. 2001, *ApJ*, 554, 1044  
 Chiappini, C., Matteucci, F., & Ballero, S. K. 2005, *A&A*, 437, 429  
 Chiappini, C., Ekström, S., Meynet, G., et al. 2008, *A&A*, 479, L9  
 Cicone, C., Bothwell, M., Wagg, J., et al. 2017, *A&A*, 604, A53  
 Contini, M., & Aldrovandi, S. M. V. 1983, *A&A*, 127, 15  
 Contini, M., & Aldrovandi, S. M. V. 1986, *A&A*, 168, 41  
 Contini, M. 2015, *MNRAS*, 452, 3795  
 Contini, M. 2016, *MNRAS*, 460, 3232  
 Contini, M. 2017a, *MNRAS*, 466, 2787  
 Contini, M. 2017b, *MNRAS*, 469, 3125  
 Contini, M. 2018, *arXiv:1801.03312*  
 Costa, R. D. D., Uchida, M. M. M., & Maciel, W. J. 2004, *A&A*, 423, 199  
 Cresci, G., Mannucci, F., Maiolino, R., et al. 2010, *Nature*, 467, 811  
 Cucchiara, A., Fumagalli, M., Rafelski, M., et al. 2015, *ApJ*, 804, 51  
 Deharveng, L., Peña, M., Caplan, J., & Costero, R. 2000, *MNRAS*, 311, 329  
 De Masi, C., Matteucci, F., & Vincenzo, F. 2018, *MNRAS*, 474, 5259  
 Dopita M. A., Kewley L. J., Sutherland R. S., Nicholls D. C., 2016, *Ap&SS*, 361, 61  
 Ellison, S. L., Simard, L., Cowan, N. B., et al. 2009, *MNRAS*, 396, 1257  
 Esteban, C., García-Rojas, J., Peimbert, M., et al. 2005, *ApJ*, 618, L95  
 Esteban, C., Fang, X., García-Rojas, J., & Toribio San Cipriano, L. 2017, *MNRAS*, 471, 987  
 Fernández-Martín, A., Pérez-Montero, E., Vílchez, J. M., & Mampaso, A. 2017, *A&A*, 597, A84  
 Garnett D. R. 1990, *ApJ*, 363, 142  
 Genovali, K., Lemasle, B., da Silva, R., et al. 2015, *A&A*, 580, A17  
 Gibson, B. K., Pilkington, K., Brook, C. B., Stinson, G. S., & Bailin, J. 2013, *A&A*, 554, A47  
 Grand, R. J. J., Bustamante, S., Gómez, F. A., et al. 2018, *MNRAS*, 474, 3629  
 Grieco, V., Matteucci, F., Pipino, A., & Cescutti, G. 2012, *A&A*, 548, A60  
 Grisoni, V., Spitoni, E., Matteucci, F., et al. 2017, *MNRAS*, 472, 3637  
 Gutenkunst, S., Bernard-Salas, J., Pottasch, S. R., Sloan, G. C., & Houck, J. R. 2008, *ApJ*, 680, 1206–1221  
 Henry, R. B. C., Edmunds, M. G., & Köppen, J. 2000, *ApJ*, 541, 660  
 Hinshaw G., Larson D., Komatsu E., et al., 2013, *ApJS*, 208, 19  
 Hopkins A. M., Beacom J. F. 2006, *ApJ*, 651, 142  
 Israelian, G., Ecuivillon, A., Reboló, R., et al. 2004, *A&A*, 421, 649  
 Izotov, Y. I., & Thuan, T. X. 1999, *ApJ*, 511, 639  
 Kacprzak, G. G., Yuan, T., Nanayakkara, T., et al. 2015, *ApJ*, 802, L26  
 Kewley, L. J., & Ellison, S. L. 2008, *ApJ*, 681, 1183–1204  
 Kobayashi C., 2004, *MNRAS*, 347, 740  
 Kobayashi C., Umeda H., Nomoto K., Tominaga N., Ohkubo T., 2006, *ApJ*, 653, 1145  
 Kobayashi C., Springel V., White S. D. M., 2007, *MNRAS*, 376, 1465  
 Kobayashi C., Nakasato N., 2011, *ApJ*, 729, 16  
 Kobayashi C., Karakas A. I., Umeda H., 2011, *MNRAS*, 414, 3231  
 Kobayashi, C. 2016, *Nature*, 540, 205  
 Korotin, S. A., Andrievsky, S. M., Luck, R. E., et al. 2014, *MNRAS*, 444, 3301  
 Kriek, M., Conroy, C., van Dokkum, P. G., et al. 2016, *Nature*, 540, 248  
 Kroupa, P., 2008, *Pathways Through an Eclectic Universe*, 390, 3  
 Luck, R. E., Gieren, W. P., Andrievsky, S. M., et al. 2003, *A&A*, 401, 939  
 Luck, R. E., & Lambert, D. L. 2011, *AJ*, 142, 136  
 Maciel, W. J., & Koppen, J. 1994, *A&A*, 282, 436  
 Madau P., Dickinson M. 2014, *ARA&A*, 52, 415  
 Magrini, L., Sestito, P., Randich, S., & Galli, D. 2009, *A&A*, 494, 95  
 Magrini, L., Gonçalves, D. R., & Vajgel, B. 2017, *MNRAS*, 464, 739  
 Matteucci, F., 1986, *MNRAS*, 221, 911  
 Matteucci, F. 1994, *A&A*, 288, 57  
 Matteucci, F. 2001, Kluwer Academic Publishers  
 Matteucci, F. 2012, Springer-Verlag Berlin Heidelberg

- Micali, A., Matteucci, F., & Romano, D. 2013, MNRAS, 436, 1648
- Mollá, M., Vílchez, J. M., Gavilán, M., & Díaz, A. I. 2006, MNRAS, 372, 1069
- Mott, A., Spitoni, E., & Matteucci, F. 2013, MNRAS, 435, 2918
- Müller, B., Heger, A., Liptai, D., & Cameron, J. B. 2016, MNRAS, 460, 742
- Nieva, M.-F., & Przybilla, N. 2012, A&A, 539, A143
- Pagel, B. E. J. 2009, Cambridge University Press
- Peng, Y.-j., Lilly, S. J., Kovač, K., et al. 2010, ApJ, 721, 193
- Pérez-Montero E., García-Benito R., Vílchez J. M., et al. 2016, A&A, 595, A62
- Pettini M., Ellison S. L., Bergeron J., Petitjean P. 2002, A&A, 391, 21
- Pettini M., Zych B. J., Steidel C. C., Chaffee F. H. 2008, MNRAS, 385, 2011
- Pilkington, K., Few, C. G., Gibson, B. K., et al. 2012, A&A, 540, A56
- Pilyugin, L. S., Vílchez, J. M., & Thuan, T. X. 2010, ApJ, 720, 1738
- Pilyugin, L. S., Grebel, E. K., Zinchenko, I. A., Nefedyev, Y. A., & Mattsson, L. 2017, MNRAS, 465, 1358
- Pipino, A., & Matteucci, F. 2004, MNRAS, 347, 968
- Portinari, L., & Chiosi, C. 1999, A&A, 350, 827
- Queyrel, J., Contini, T., Kissler-Patig, M., et al. 2012, A&A, 539, A93
- Renzini, A., & Peng, Y.-j. 2015, ApJ, 801, L29
- Rudolph, A. L., Fich, M., Bell, G. R., et al. 2006, ApJS, 162, 346
- Sánchez, S. F., Barrera-Ballesteros, J. K., Sánchez-Menguiano, L., et al. 2017, MNRAS, 469, 2121
- Sánchez-Menguiano L., Sánchez S. F., Pérez I., et al. 2016, A&A, 587, A70
- Schönrich, R., & McMillan, P. J. 2017, MNRAS, 467, 1154
- Smartt S. J., 2009, ARA&A, 47, 63
- Spite, M., Cayrel, R., Plez, B., et al. 2005, A&A, 430, 655
- Spitoni, E., & Matteucci, F. 2011, A&A, 531, A72
- Spitoni, E., Vincenzo, F., Matteucci, F., & Romano, D. 2016, MNRAS, 458, 2541
- Springel, V., Yoshida, N., & White, S. D. M. 2001, New Astron., 6, 79
- Springel V., 2005, MNRAS, 364, 1105
- Stanghellini, L., Guerrero, M. A., Cunha, K., Manchado, A., & Villaver, E. 2006, ApJ, 651, 898
- Taylor, P., & Kobayashi, C. 2014, MNRAS, 442, 2751
- Taylor, P., & Kobayashi, C. 2015a, MNRAS, 448, 1835
- Taylor, P., & Kobayashi, C. 2015b, MNRAS, 452, L59
- Taylor, P., & Kobayashi, C. 2016, MNRAS, 463, 2465
- Taylor, P., & Kobayashi, C. 2017, MNRAS, 471, 3856
- Maior, U., & Tescari, E. 2015, MNRAS, 453, 3798
- Thomas, D., Maraston, C., & Bender, R. 2003, MNRAS, 339, 897
- Vangioni, E., Dvorkin, I., Olive, K. A., et al. 2017, preprint (arXiv:1710.10075)
- Ventura, P., Di Criscienzo, M., Carini, R., & D'Antona, F. 2013, MNRAS, 431, 3642
- Ventura, P., Stanghellini, L., Dell'Agli, F., & García-Hernández, D. A. 2017, MNRAS, 471, 4648
- Vila Costas, M. B., & Edmunds, M. G. 1993, MNRAS, 265, 199
- Vincenzo F., Belfiore F., Maiolino R., Matteucci F., Ventura P., 2016a, MNRAS, 458, 3466
- Vincenzo, F., & Kobayashi, C. 2018, A&A, 610, L16
- Werk, J. K., Putman, M. E., Meurer, G. R., et al. 2010, ApJ, 715, 656
- Zafar, T., Centurión, M., Péroux, C., et al. 2014, MNRAS, 444, 744
- Zoccali, M., Hill, V., Lecureur, A., et al. 2008, A&A, 486, 177